

Mechanics of the Contact Area Between a Violin Bow and a String. Part II: Simulating the Bowed String

R. Pitteroff and J. Woodhouse*

Cambridge University Engineering Department, Trumpington St, Cambridge CB2 1PZ, U.K.

Summary

A simulation model of the bowed string incorporating the finite width of the bow, the longitudinal compliance of the bow-hair and the torsional motion of the string is developed and explored. It is based on the mathematical model developed in a companion paper [1] to this, describing the contact mechanics of string and bow in a regime of sticking. In-depth comparisons between point-bow and finite-width calculations reveal significant differences in a number of important details. The waveforms of musically relevant oscillation regimes are modified. The physical basis for these results is elucidated in some detail.

PACS no. 43.75.De, 43.40.Cw

1. Introduction

The first step toward a simulation model of the bowed string taking into account the finite width of the bow was taken in Part I [1] of this set of papers, where the interaction of a bow of finite width and a string was studied in a regime in which the string is permanently in *sticking* contact with the hair of a stationary bow. In this paper that theory of the contact of bow and string is applied to the simulation of the self-excited motion of a bowed string, where episodes of stick and slip alternate. In Part I the linear problem of the string sticking to the bow was treated with analytical methods. Here, the nonlinearity of the frictional behaviour of the stick-slip process calls for numerical methods. We will focus on situations when the string is executing “Helmholtz motion”, or a close approximation to it, in order to see how this motion is affected by the physical ingredients studied in Part I, namely the finite width of the bow, the longitudinal compliance of the bow-hair, the torsional motion of the string and the bending stiffness of the string.

Of the many possible patterns of vibration of a bowed string, Helmholtz motion is the one which is generally musically acceptable. In Helmholtz motion the shape of the string consists of two rather straight sections joined by a corner, the “Helmholtz corner”, performing round trips on the string (Figure 1). Helmholtz motion involves a single episode of slipping and one of sticking during each period, the transitions between the two frictional states being triggered by the passage past the bow of the corner. While the corner is travelling from the bow to the nut or the finger stop and back to the bow (positions 1–5 in Figure 1) the string is sticking to the bow and is carried forward with the bow velocity v_b . Having completed the right-hand part of its round trip the corner strikes the bow and triggers “release” (stick-to-slip transition) of the string by increasing the restoring force of the string beyond the threshold of limiting friction. Slipping

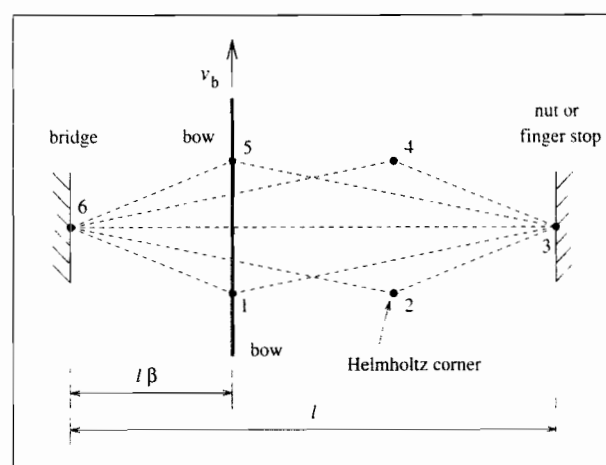


Figure 1. Idealised Helmholtz motion. Consecutive snapshots of the shape of the string during one full period. The bowing position β is expressed as usual as a fraction of the string length l . The bow velocity is v_b .

persists while the corner is travelling to the bridge and back to the bow (positions 5–1) when “capture” (slip-to-stick transition) of the string takes place.

The type of motion in which the string shape consists of perfectly straight lines (idealised Helmholtz motion) is a solution to the hypothetical system of a perfectly flexible string rigidly terminated and bowed in a single point by a rigid bow. The top trace of Figure 2 is the waveform of the string centre-line velocity, as it would be observed under the bow, in idealised Helmholtz motion.

The middle diagram indicates the alternating episodes of slipping and sticking friction between string and bow. The bottom trace is the idealised waveform of the transverse force exerted by the string on the bridge. In idealised Helmholtz motion it is identical in shape with the velocity waveform of the left-bound travelling wave. The bridge force is a meaningful signal since it is the force driving the sound-radiating body of the violin. It is also a very useful signal from a practical point of view since it can be measured fairly reliably with an arrangement of piezo-electric transducers lining the

Received 17 June 1996.

accepted 17 September 1997.

* To whom correspondence should be sent

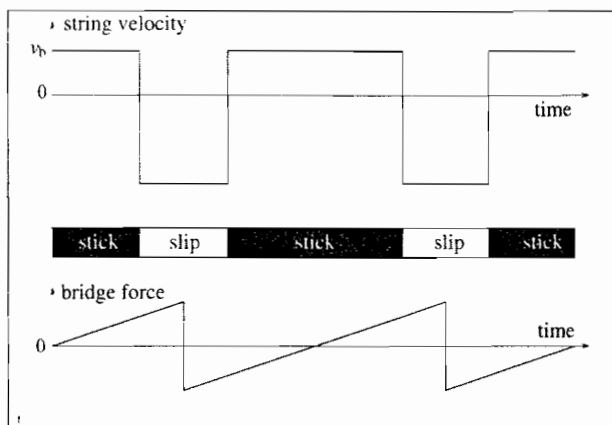


Figure 2. Idealised Helmholtz motion. Top: waveform of the transverse string centre-line velocity. Middle: alternation of slipping and sticking friction. Bottom: waveform of the transverse force which the string exerts on the bridge.

string notch on the bridge [2]. In the present simulations no attempt is made to model the physical behaviour of the bridge accurately, and the waveform of the travelling wave which emanates from the inner edge of the bow will be referred to as the "bridge-force waveform".

In reality, Helmholtz motion can only be an approximation to the idealised case. Rounding-off of the waveform through various dissipative and dispersive mechanisms determines the detailed shape of the waveforms (see for example Cremer [3] or McIntyre *et al.* [4]). More significantly for the present investigation, the finite width of the bow is incompatible with idealised Helmholtz motion. The transitions from one frictional state to the other are not instantaneous as suggested by the middle diagram of Figure 2, but presumably each bow-hair has its own release and capture events. The incompatibility can be visualised using a sketch, Figure 3, reproduced from McIntyre *et al.* [5]. The argument is based on idealised Helmholtz motion.

In position 1, the Helmholtz corner has just travelled past the bow from left to right. While the entire section of the string under the bow sticks to the bow-hair, it is carried forward parallel to its initial position. This produces additional kinks at the edges of the bow, as seen in position 2. The string shape of idealised Helmholtz motion which would follow from a single point bow applied to the string at $x = l\beta_0$ is given by the dashed line.

The additional kinks lead to restoring forces and corresponding friction forces F_i and F_o as indicated in Figure 3(b), where a constant slope has been subtracted out from position 2. These forces can build up to a level which forces at least part of the string under the bow to slip for a time: so-called "differential-slipping events" [5] or "partial slips". The forces are of opposite sign, so that there is a tendency for bow hairs near the bridge to slip backwards relative to the bow motion, in the same sense as the main Helmholtz slip. Hairs on the opposite side of the bow, by contrast, tend to slip forwards relative to the bow motion. Various degrees of differential slipping might occur: very localised partial slips which relieve local temporary peaks in friction force and

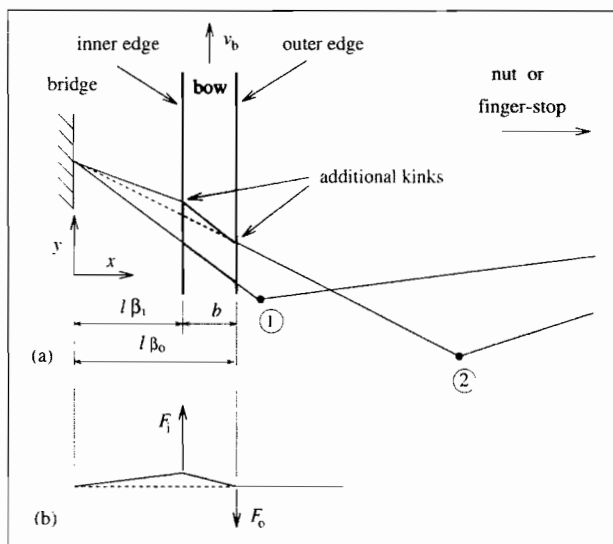


Figure 3. Schematic representation of the incompatibility of idealised Helmholtz motion and finite bow width. Idealised Helmholtz motion requires the string to move from position 1 to the position given by the dashed line, whereas uniform bow velocity across the width of the bow produces the shape given by the solid line. All displacements are drawn exaggerated.

thereby allow Helmholtz motion to persist, or more drastic events with effects detrimental to Helmholtz motion. Especially when bowing close to the bridge one can observe noise-generating spikes in the bridge-force waveform during the nominal sticking phase, and these spikes can be traced back to differential-slipping events [5].

In practice, there are two factors which might allow Helmholtz motion to persist despite the incompatibility just discussed: these are torsional motion of the string, and the finite compliance of the bow-hair. Either might alleviate the additional forces at the edge of the bow. Such effects will be studied in this paper.

This paper is structured in the following way: the mathematical treatment of the bowed string is dealt with in Section 2.1. Having argued in Part I that finite width and bow-hair compliance are the most important ingredients of an enhanced simulation model, numerical methods for a model neglecting finite bending stiffness of the string will be developed at first (Section 2.2). The methods required for the stiff string, somewhat more involved than those for the perfectly flexible string, follow in Section 2.3. Section 3 deals with fundamental tests of the simulation methods and in Section 4 some simulation results are discussed.

2. Methods

2.1. Theoretical model

For the present simulation model the bow stick is regarded as a rigid frame moving at a given velocity v_b and supporting a ribbon of compliant bow-hair. The bow-hair itself is thought of as a massless elastic support with velocity proportional damping; this is the simple "spring-dashpot" bow model

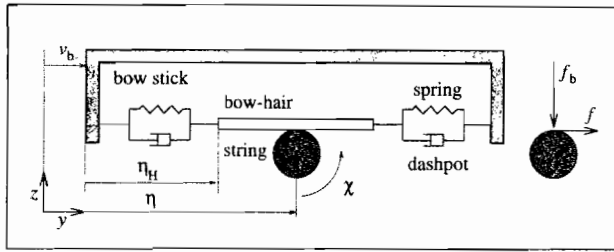


Figure 4. Definition of frame of reference and coordinates.

shown in Figure 4. Theoretical predictions for the reflection and transmission problem based on this model of material behaviour were shown in Part I to match experimental results well.

The displacement η of the string centre-line, the angular displacement χ and the velocity v_b of the bow stick are defined in a coordinate system at rest with respect to the violin (Figure 4). The displacement η_H of the bow-hair at the contact of string and bow is defined relative to the bow stick. The normal force f_b (henceforth "bow force") and the friction force f , both distributed quantities acting on the string, are defined to be positive when oriented as shown in Figure 4. The relative velocity v_{rel} is defined as the difference in velocity between the string surface and the surface of the bow-hair on the line of contact,

$$v_{rel} = \left(\frac{\partial \eta}{\partial t} - a \frac{\partial \chi}{\partial t} \right) - \left(v_b + \frac{\partial \eta_H}{\partial t} \right), \quad (1)$$

where a denotes the radius of the string. Longitudinal string deformation, coupling of transverse waves in the two planes and coupling of transverse and torsional waves on the free string are neglected. Effects due to motion in the perpendicular plane will be discussed in a companion paper (Part III [7]). The bow velocity v_b is chosen to be positive throughout.

The governing equations for the motion of the string under the bow are the equations of momentum (2) and angular momentum (3). They are coupled through the distributed friction force f . This force also appears in the constitutive relation given by equation (4), where it is linked to the bow-hair displacement η_H . The distributed spring and damping constants are denoted s and d respectively. The relative velocity is expressed in equation (5). The five quantities, η , χ , η_H , f and v_{rel} are functions of the space coordinate x and time t . A fifth equation is needed to close the system of equations. During *stick* this is the rolling constraint given in the first of equation (6), which leads to a system of five linear equations. During *slip*, a friction curve provides the fifth equation as in the second of equation (6).

$$T \frac{\partial^2 \eta}{\partial x^2} - B \frac{\partial^2 \eta}{\partial x^4} + f = m \frac{\partial^2 \eta}{\partial t^2}, \quad (2)$$

$$K \frac{\partial^2 \chi}{\partial x^2} - a f = \Theta \frac{\partial^2 \chi}{\partial t^2}, \quad (3)$$

$$f = -s \eta_H - d \frac{\partial \eta_H}{\partial t}, \quad (4)$$

$$v_{rel} = \left(\frac{\partial \eta}{\partial t} - a \frac{\partial \chi}{\partial t} \right) - \left(v_b + \frac{\partial \eta_H}{\partial t} \right), \quad (5)$$

$$v_{rel} = 0 \text{ (stick)} \quad \text{or} \quad f = \mu f_b \text{ (slip)}. \quad (6)$$

The coefficient of dynamic friction μ is a function of one or more state variables, depending on the particular friction model one chooses to use. Thus there are two different sets of equations describing the action of the string according to whether, at a given time at a given point under the bow, the string is sticking or slipping. The algorithm used in simulating the bowed string has to switch back and forth between these.

The mathematical treatment of the bowed string in contact with a bow over a finite section of its length involves joining together domains of very different character. On the section of string beneath the bow, the problem is nonlinear and the solution has to be sought numerically. On the sections of free string, however, the behaviour is governed by two uncoupled ordinary wave equations (for the transverse and the torsional motion). For these, travelling-wave solutions can be employed. The reflection of waves at the terminations of the string ("bridge" will stand for the near end of the string, "nut" will stand for the far end of the string which could also be a finger-stop) can be dealt with by convolution with appropriate reflection functions as described in [4].

The exact nature of the frictional behaviour between string and bow-hair is still unknown. Lazarus [8] provided the first qualitative measurement of the frictional behaviour and more recently J.H. Smith [9], in an extensive study of rosin friction, has shown that the friction forces between rosined surfaces depend on the history of the contact. Here a rather simplistic friction law is assumed, in which the coefficient of dynamic friction at a given point under the bow depends solely on the instantaneous value of the relative velocity at this point. This model probably does not represent real frictional behaviour very accurately, but it is the model most commonly used and is well suited to the present investigation.

When the relative velocity is zero, there is sticking friction and the friction force f may take any value $f \in [-\mu_s f_b, \mu_s f_b]$, where μ_s is the coefficient of (limiting) static friction. When the relative velocity v_{rel} is non-zero, μ is assumed to vary according to

$$\mu(v_{rel}) = \pm \left[\mu_d + \frac{(\mu_s - \mu_d) v_0}{v_0 \mp v_{rel}} \right]. \quad (7)$$

This is the rectangular hyperbola illustrated in Figure 5. The asymptotic value of the coefficient of dynamic friction is μ_d and v_0 is a constant. Note that, because the velocity of the bow-hair surface is not identical to the bow velocity, it is advantageous to express μ as a function of the relative velocity and not, as is commonly done, as a function of the string centre-line velocity. (The alternative signs in equation (7) apply for situations in which $v_{rel} > 0$, i.e. the string surface is slipping forwards relative to the bow-hair surface.) The left-hand branch of the friction law is defined by: a vertical asymptote at $v_{rel} = v_0$, a horizontal asymptote at $\mu = \mu_d$, and $\mu = \mu_s$ for $v_{rel} = 0$. (As a consequence $\mu = (\mu_s + \mu_d)/2$ for $v_{rel} = -v_0$.) In the first instance it is assumed that the same friction law applies for both concentrated point-bow forces and distributed finite-width forces.

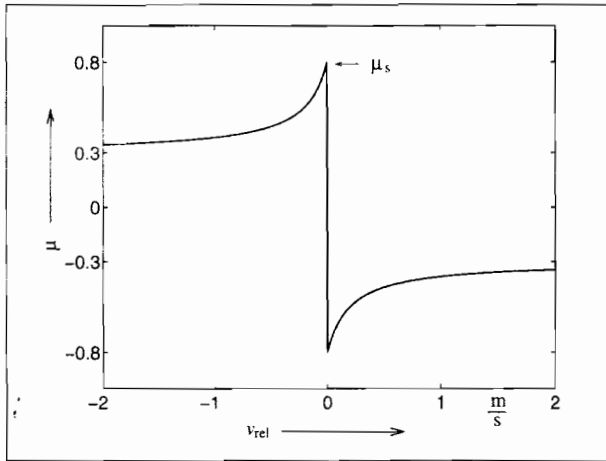


Figure 5. The friction law used in the simulations: $\mu_s = 0.8$, $\mu_d = 0.3$ and $v_0 = 0.2$ m/s.

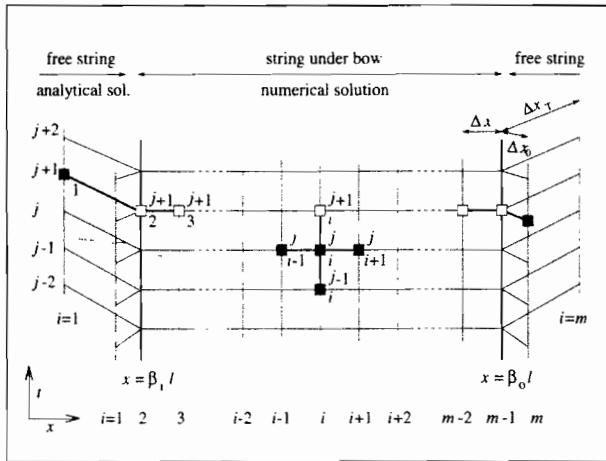


Figure 6. The discretisation grid used for the numerical simulation of the perfectly flexible bowed string.

2.2. Numerical methods I: The perfectly flexible string

Time-domain approaches have proved more useful for modelling of the action of the bowed string than frequency-domain approaches. The simplest method, an explicit time-stepping method, gives the most insight into the physical processes. Implicit schemes would be rather difficult to implement because at each discrete position under the bow it has to be decided individually at each time step whether the string is sticking or slipping. The present finite-difference method is based on the discretisation grid shown in Figure 6. The section of the string under the bow runs from the left interface at $x = \beta_1 l$ to the right interface at $x = \beta_0 l + b$, or in terms of the discretisation grid, from grid-point $i = 2$ to $i = m - 1$. Grid-points $i = 1$ and $i = m$ belong to the outer, analytical solution of the free string. The displacement values at these grid-points are found by superposition of the known incoming waves and the known outgoing waves emanating from the interface grid-points. Separate grid-points are used for the transverse and the torsional motion, since the corresponding waves propagate independently on the string.

Because the outer solution is analytical it is adequate to choose the grid-spacing in the outside region to be the product of the time step Δt and the transverse or the torsional wave speed c_0 or c_T on the free string: $\Delta x_T = c_T \Delta t$ is typically larger than $\Delta x_0 = c_0 \Delta t$. The difference in grid-spacing for the two types of motion is shown in Figure 6 by splitting the grid in the outer domain and folding it apart. The displacement values of the outgoing waves at grid-points $i = 1$ and $i = m$ at a given time step are simply the values at the interface grid-points at the previous time step.

Under the bow the transverse and torsional motions are coupled through the friction force, and therefore one single discretisation grid is used. Equations (2)–(6) describing the action of the string under the bow are discretised using standard two-point difference approximations for first derivatives and three-point central-difference approximations for second derivatives. The stiffness term in equation (2) is omitted. The resulting finite-difference equations are given in ref. [10]. The stencil is visualised at the centre of Figure 6. The new displacement values are represented by white squares. Values of string and hair displacement of two previous time levels, represented by black squares, must be stored.

For the grid-points at the interfaces of free string and string under the bow we have a choice of methods. One can either extend the finite-difference scheme into the free string to encompass the interface grid-points, or rewrite the jump conditions in terms of finite-difference equations as well. Here the second method is chosen because it allows reduction to a point-bow model. For the case of the stiff string we will resort to the first method.

The jump conditions for an interface at $x = x_0$ are:

$$[\eta]_{-x_0}^{+x_0} = 0, \quad (8)$$

$$[\chi]_{-x_0}^{+x_0} = 0, \quad (9)$$

$$[\eta_x]_{-x_0}^{+x_0} = 0, \quad (10)$$

$$[\chi_x]_{-x_0}^{+x_0} = 0. \quad (11)$$

The continuity in η and χ is automatically fulfilled since each interface is represented by one grid-point only. The two non-trivial jump conditions equations (10)–(11) are discretised using two-point backward and forward approximations. Equations (10)–(11) together with equations (4)–(6), all in their discretised form, constitute a system of five equations for the new values of the five quantities η , η_H , χ , f and v_{rel} at the interface.

The new displacement values are calculated in the following order: first the displacements at grid-points $i = 1$ and $i = m$ from the analytical solution on the free string, then the internal grid-points $i = 3$ to $i = m - 2$ and finally the interface grid-points $i = 2$ and $i = m - 1$.

The methods just described can be adapted to model a point contact of bow and string for comparison with other point-bow simulation methods. The changes are made in the interior, numerical domain only, whilst the treatment of the outer solution remains unchanged. The two interfaces

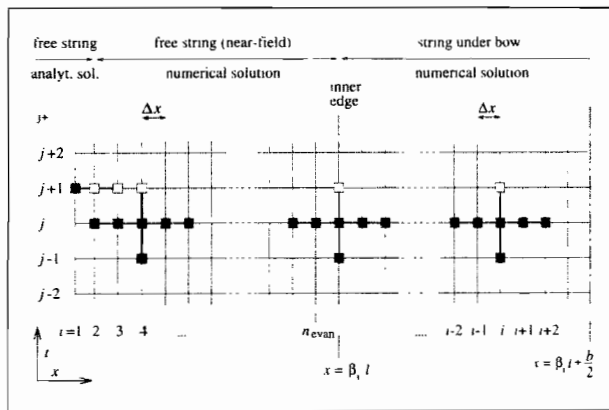


Figure 7. The discretisation grid used for the numerical simulation of the stiff string.

collapse so that at the point of contact $x = x_0$ the following jump conditions must be satisfied:

$$[\eta]_{-x_0}^{+x_0} = 0, \quad (12)$$

$$[\chi]_{-x_0}^{+x_0} = 0, \quad (13)$$

$$T[\eta_x]_{-x_0}^{+x_0} = -F, \quad (14)$$

$$K \left[\chi_x \right]_{-x_0}^{+x_0} = a F. \quad (15)$$

The continuity in η and χ is automatically fulfilled since the point of contact is represented by just one grid-point. The remaining equations describing the action of string and bow are equation (5) expressing the relative velocity, and lumped versions of equations (4) and (6), where the distributed quantities f , f_b , s and d are replaced by F , F_b , S and D .

Rigorous proofs of stability and convergence for these complex finite-difference schemes are neither easily performed nor essential. One can only carry out theoretical stability and convergence investigations of the finite-difference scheme for the linear branch of the problem, the string sticking to the bow, as general stability and convergence criteria are not known for nonlinear problems. However, elementary empirical tests of stability and convergence have shown satisfactory behaviour.

2.3. Numerical methods II: The stiff string

When modelling bending stiffness the equation of momentum (2) includes an additional term, and a different set of jump conditions at the interfaces of free string and string under the bow must be satisfied. The fourth derivative with respect to x is modelled with a five-point central-difference formula. The finite-difference method is based on the discretisation grid visualised in Figure 7. The grid is symmetric about the mid-point of the bow, so only the left half of the grid is shown. Grid-points $i = 1$ to $i = n_{\text{evan}}$ represent the free string while the grid-points from $i = n_{\text{evan}} + 1$ onwards represent the section of the string under the bow.

The numerical methods derived for the perfectly flexible string must be upgraded in several ways. Firstly, the interaction of bow and string can only be described by taking the transverse near-fields on either side of the bow into account. These near-fields are the result of the evanescent waves arising from the bending stiffness. The finite-difference scheme for transverse motion of the string must therefore be extended into the free string to encompass the exponentially decaying evanescent waves generated at the interfaces. Typically an extension of the finite-difference scheme by a bow width on both sides is found to be sufficient. Secondly, to ensure numerical stability the jump conditions at the interfaces of free string and string under the bow are no longer explicitly expressed as finite-difference equations. They are now satisfied by means of a continuous finite-difference scheme in which the coefficients change at the interfaces. Also, for reasons of numerical stability, the jump conditions used to match the domain covered by the finite-difference scheme with the outer, analytical solution assume a perfectly flexible string at the boundaries of the finite-difference scheme, i.e. the string at grid-points $i = 1$ to $i = 3$ is assumed to be perfectly flexible. The transverse and torsional displacement values at $i = 1$ are obtained by superposition of the known incoming and outgoing waves as above. The transverse displacement at grid-point $i = 3$ is calculated using a finite-difference stencil without the stiffness term. The displacements at $i = 2$ are then obtained by discretisation of the continuity conditions

$$[\eta_x]_{-x_0}^{+x_0} = 0, \quad (16)$$

$$[\chi_x]_{-x_0}^{+x_0} = 0. \quad (17)$$

The full "stiff" treatment of the string begins with grid-point $i = 4$. Thirdly, the waves travelling to the string terminations and back suffer dispersion due to bending stiffness. This effect can be modelled through suitable reflection functions such as those described by Woodhouse [11]. Here the interest is in investigating the hitherto unknown effects of bending stiffness in the vicinity of the bow only, and therefore dispersive effects due to stiffness on the free string beyond the near-fields are not included in the simulations. Note that because the finite-difference scheme is interfaced with the outer analytical solution assuming a perfectly flexible string at the boundary and the interfaces between free string and string under the bow are treated with a continuous scheme, there is no singularity for $B \rightarrow 0$. Therefore the "stiff model" can be employed for calculations of the perfectly flexible case as well.

Numerical simulation methods for the stiff string are more prone to numerical instabilities than methods for the perfectly flexible string. Various smoothing schemes exist but as smoothing may obscure physical effects, such a scheme has not been implemented here. For very small bridge-bow distances the near-field generated at the inner edge of the bow has a non-negligible amplitude at the bridge. In this case it would be advisable to use a finite-difference scheme which includes the entire section of the string between bridge and

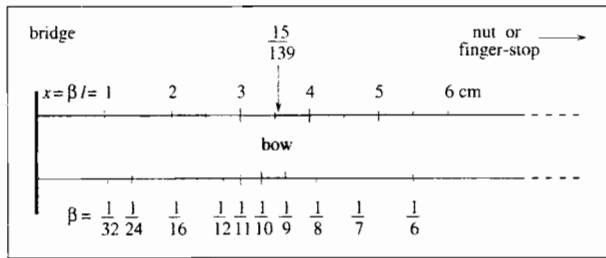


Figure 8. Schematic representation of the position of the finite-width bow.

bow and the bridge itself. For point-bow simulations one simply reduces the number of grid-points under the bow whilst keeping the remainder of the finite-difference scheme unchanged. To achieve numerical stability the bow must be represented by more than one grid-point.

3. Simulation parameters and tests

3.1. Model string and bow

The model string used for all the examples in this paper has parameter values typical of a violin A string with nominal frequency 440 Hz. This string has a characteristic impedance for transverse motion of $Z_0 = 0.2 \text{ kg/s}$, a ratio of torsional to transverse impedance of $Z_T/Z_0 = 1.6$, a transverse phase velocity of $c_0 = 289.5 \text{ m/s}$ and a ratio of torsional to transverse phase velocities of $c_T/c_0 = 2.4$. The string radius is $a = 0.34 \text{ mm}$ and its length is $l = 0.329 \text{ m}$.

The bow velocity is $v_b = 0.2 \text{ m/s}$. The friction law is defined by the coefficients of static and asymptotic dynamic friction $\mu_s = 0.8$ and $\mu_d = 0.3$ and $v_0 = 0.2 \text{ m/s}$. The friction law in Figure 5 is based on these values. The bow-compliance parameters are based on the contact of string and bow lying at the mid-point of the bow lengthwise. Allowing for other positions on the bow would however present no obstacle. For the reference case the model bow has a width of $b = 10 \text{ mm}$ and distributed spring and damping constants of $s = 6 \times 10^6 \text{ (N/m)/m}$ and $d = 1000 \text{ (kg/s)/m}$. The mid-point of the bow widthwise is placed at the relative position $\beta = 15/139$. Thus the bow covers a section of string ranging roughly from $\beta = 1/11$ to $\beta = 1/8$ (Figure 8).

The reference case features a bow force of $F_b = 0.4 \text{ N}$ or $f_b = 40 \text{ N/m}$. To put this into perspective, we may calculate the theoretical maximum acceptable bow force which still allows Helmholtz motion. It is calculated according to Schelleng's rule ([12], see also Schelleng's footnote 10), extended by Schumacher [13] to take into account torsional motion:

$$F_{bS} = \frac{2Z_0 \frac{Z_T}{Z_0 + Z_T} v_b}{(\mu_s - \mu_d)\beta} \quad (18)$$

The predictions for a point bow located at the inner edge, the mid-point and the outer edge of the finite-width bow are $F_{bS} = 1.06, 0.91, 0.80 \text{ N}$. We will refer to calculations based on equation (18) as the Schelleng maximum bow force.

Our standard time resolution is 2780 time steps per nominal period T_0 . Thus the sampling frequency is $440 \times 2780 \text{ Hz}$, well above the usual audio frequency of 44.1 kHz. Our standard spatial resolution under the bow uses a grid-spacing of $\Delta x = 1 \text{ mm}$, that is 11 grid-points make up a bow of 10 mm width. The first and the last grid-point represent sections of string at the edges, half free string, half string under the bow, which must be kept in mind when comparing finite-width and point-bow results.

The Gaussian $\exp(-u^2)$ with $u \in [-1.5, 1.5]$ is used as the generic reflection function. The Gaussian is evaluated at a number r of equidistant values u_j , where r is the number of time steps corresponding to the time interval $0.05 T_0$ for the transverse and $0.05 T_0 (c_0/c_T)$ for the torsional reflection functions respectively. The precise values u_j of each series depend on the required time-delays. The resulting series $\exp(-u_j^2)$ are normalised such that the sum of each series is -1 . This symmetric, artificially featureless reflection function is chosen to make it easier to associate details of waveforms with the new effects being modelled here, with minimal confusion.

The results shown here are from simulations which were started from idealised Helmholtz waveforms (although quiescent initial conditions present no difficulty) and run until a solution sufficiently close to steady state was attained. Usually results from periods 49 and 50 are shown. In all cases presented in this paper the full-width bow is assumed to lie flat on the string.

3.2. Test 1: Pitch fidelity

The truncation errors inherent to numerical schemes lead to unavoidable inaccuracies. One particular consequence is that the numerical phase velocity of a finite-difference scheme differs from that of the physical system it is modelling, and this difference is usually frequency dependent. However, the degree of numerical pitch change can easily be assessed in a numerical experiment using the simulation model with the friction force turned off. Over a wide range of parameter values this effect was found to be negligible. Only for cases with implausibly high values of bending stiffness was the degree of numerical pitch distortion found to be noticeable.

3.3. Test 2: Reflection and transmission problem

The reflection and transmission problem — transverse waves propagating on an infinite string and interacting with a bow at rest placed on the string — studied in Part I is not only an interesting case in itself but can also provide a test of the simulation methods. In the real experiment a bow force F_b is applied to the string sufficient to ensure sticking everywhere in the contact zone. To model this, one simply disallows slipping in the simulation model. For the model string and bow described above we compare analytically and numerically calculated transverse and torsional reflection and transmission coefficients. The string is assumed to be perfectly flexible. In the undamped case excellent agreement in all four coefficients is found for harmonic numbers up to

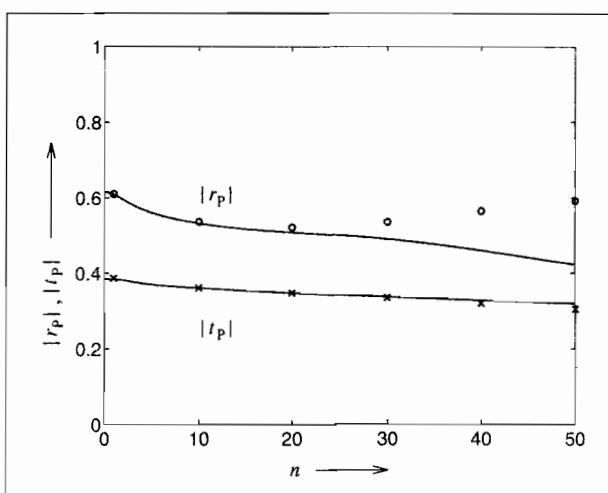


Figure 9. Comparison of analytical and numerical results. Reflection and transmission problem for the "infinite" string in contact with a compliant finite-width bow at rest. Transverse reflection and transmission coefficients r_P and t_P versus harmonic number n . Analytical results are represented as solid lines, numerical results as (o) and (x). String and bow data as given in Section 3.1.

$n = 50$. Energy conservation is satisfied to within 1%. In the damped case ($d = 1000 \text{ (kg/s)/m}$) for which the reflection and transmission coefficients are shown in Figure 9 the differences between analytical and numerical results are larger. Good agreement is found for harmonic numbers up to $n = 25$. The biggest discrepancy occurs for the transverse reflection coefficient. This discrepancy vanishes when the spatial grid-spacing under the bow is refined so that $\Delta x \rightarrow 0$. Higher temporal resolution has little influence. The explanation for this behaviour is as follows. The undamped bow presents a vanishing impedance to the string as the frequency of the incident wave goes to infinity. If the temporal and spatial resolution is sufficient to describe the waves on the free string it is also sufficient to describe the string under the bow. However, on a damped bow high-frequency incident waves lead to concentrated near-fields at the edges of the bow. To resolve these adequately requires higher spatial resolution than for the waves on the free string. Inadequate spatial resolution results in a model bow with an increased impedance and therefore leads to higher values of the transverse reflection coefficient.

3.4. Test 3: Comparison with standard point-bow model

A comparative investigation has been carried out employing the point-bow model described here and the algorithm described in [4] in a version taking into account torsional effects. Excellent agreement was obtained when high resolution was used in both cases. For nearest equivalence the point-bow model described here was turned into a quasi-rigid model by choosing a very high bow-hair impedance. The string centre-line velocity at the bowing point, the bridge-force waveform and its spectrum, and the period and the durations of the sticking and slipping phases were all compared.

4. Results

4.1. General features of finite-width simulations

We now turn to the results of finite-width bowed-string simulations. We present various types of output which highlight different aspects of the behaviour. The top and the bottom graphs of Figure 10 are the familiar waveforms of the string centre-line velocity v_c , at the outer edge (top) and the inner edge (bottom) of the bow. The time window is $2T_0$. The strong fluctuations in the velocity waveform at the inner edge correspond to vigorous partial slips, discussed in more detail below. A very useful way of presenting finite-width results is in a "friction map": the middle graph in Figure 10 is such a map showing the nature of the frictional contact across the width of the bow as it varies in time. The vertical axis of the diagram represents position on the bow between the inner edge (bottom) and the outer edge (top). Black areas mark sticking contact while white and grey areas mark backward (normal) and forward slipping respectively.

We can identify the main phases of nominal slipping and nominal sticking of the Helmholtz motion, and transition phases between the two. The Helmholtz corner, approaching the outer edge towards the end of the nominal sticking phase, generates an additional friction force on top of the friction force distribution which has evolved during the nominal sticking phase. Release of the string takes place wherever the sum of both exceeds limiting friction, and not necessarily at the outer edge first. Gradually the entire string section "un-zips" and begins to slip from the bow. This is seen in the close-up representation of the release and capture events in Figure 11.

The subsequent arrival of the Helmholtz corner, after its reflection at the bridge, "re-zips" the string to the bow. Depending on the details of the bowing regime, the duration of release and capture transitions can be shorter or longer than b/c_0 , the time it takes a transverse signal to travel the distance b on the free string. Typically capture takes half as long as release. The mechanisms of release and capture are investigated in more detail in Part III.

Returning to Fig 10; the nominal sticking phase between the two main slips is interrupted by partial slips on both sides of the bow. The "incompatibility" of bow and string velocity (see Figure 3) leads to a particular distribution of the friction force. The waveforms of the local friction force at the inner and the outer edge are shown, in the two traces immediately below and above the friction map respectively. While at the inner edge a positive friction force builds up which reaches limiting friction leading to backward partial slips, at the outer edge the friction force is of opposite sign leading to forward partial slips. This is all in accordance with expectations based on Figure 3. The difference in behaviour of the two edges is also visible in the waveforms of the string centre-line velocity. More will be said about the mechanisms involved in the generation of partial slips in Section 4.2.

A visualisation of the displacement of the section of string under the bow is shown in Figure 12. Successive "snapshots" of the centre line of this string section are taken at intervals of

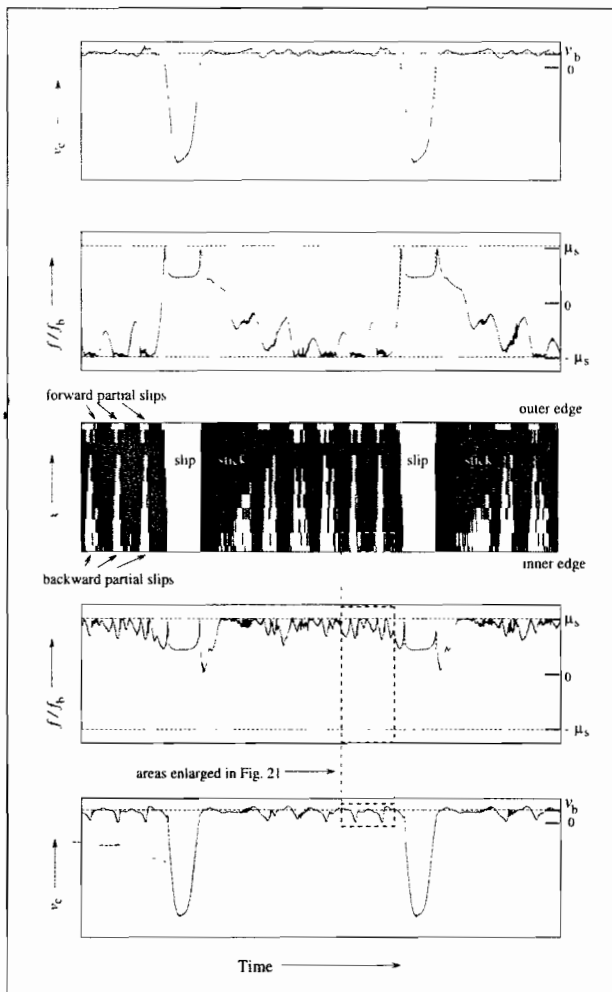


Figure 10. Typical output from a finite-width simulation. The top and the bottom traces represent the string centre-line velocity v_c at the outer and the inner edge respectively. The adjacent traces represent the normalised friction force f/f_b at the edges of the bow. The thresholds of limiting friction are indicated as $\pm\mu_s$. The central graph is a friction map showing the distribution of stick and slip across the width of the bow. Time window $2T_0$. The dashed box represents the area enlarged in Figure 20.

$1/75$ of the nominal period. For reference the corresponding steady displacement of the bow is given by the "rulers" on the margins. Figure 12(a) shows the string during the sticking phase. At the outer edge the string is transported in a rather regular way with a velocity close to the bow velocity. The displacement increments between subsequent snapshots are of similar magnitude. At the inner edge, however, the string is seen to be transported in an irregular fashion: episodes with large displacement increments alternate with episodes in which the string does not move forward at all. The latter episodes are the partial slips through which the built-up localised peaks in friction force are relieved. Their effects are strongest at the inner edge. Towards the centre of the bow the string experiences slipping as well, but remains in forward motion. The point under the bow where on average the string centre-line velocity equals the bow velocity is located very close to the outer edge of the bow in this case. Figure 12(b) relates to the slipping phase. Once the full section of string

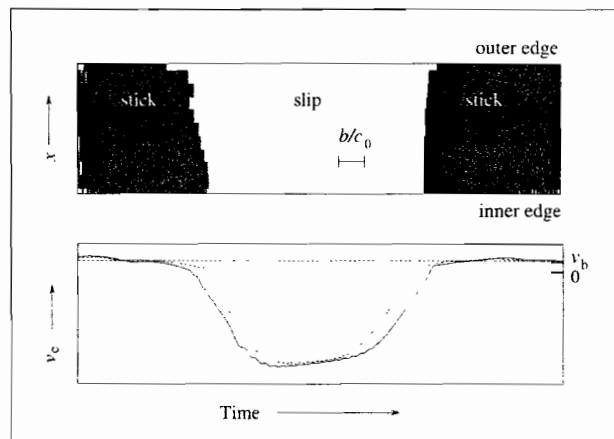


Figure 11. Close-up view of release and capture. String centre-line velocity v_c at outer (solid line) and inner edge (dashed line). Time window $0.3T_0$.

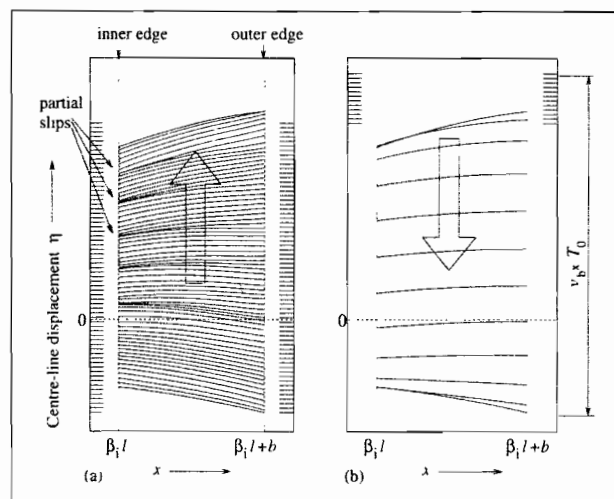


Figure 12. Consecutive snapshots of the centre-line of the section of string under the bow during one period: (a) during stick, (b) during slip. The "rulers" on the margins represent the displacement of the bow at velocity v_b .

under the bow has released from the bow the velocity is rather uniform across the width of the bow.

Figure 13 shows a series of friction maps and corresponding bridge-force waveforms for different values of the bow force F_b , the bowing position remaining the same as before. At very low bow force the string slips at the edges throughout the period and only a narrow section of the string under the bow experiences the typical alternation pattern of stick and slip once per period. The width of the section of string in sticking friction increases with bow force while the number of partial slips per period decreases. The degree of incompatibility is governed purely by geometry, independent of bow force. The same is true of the consequential build-up of the friction forces at the edges. A higher bow force, however, increases the threshold of limiting friction. Thus the tendency to partial slips does not depend on bow force, but the precise pattern of them does.

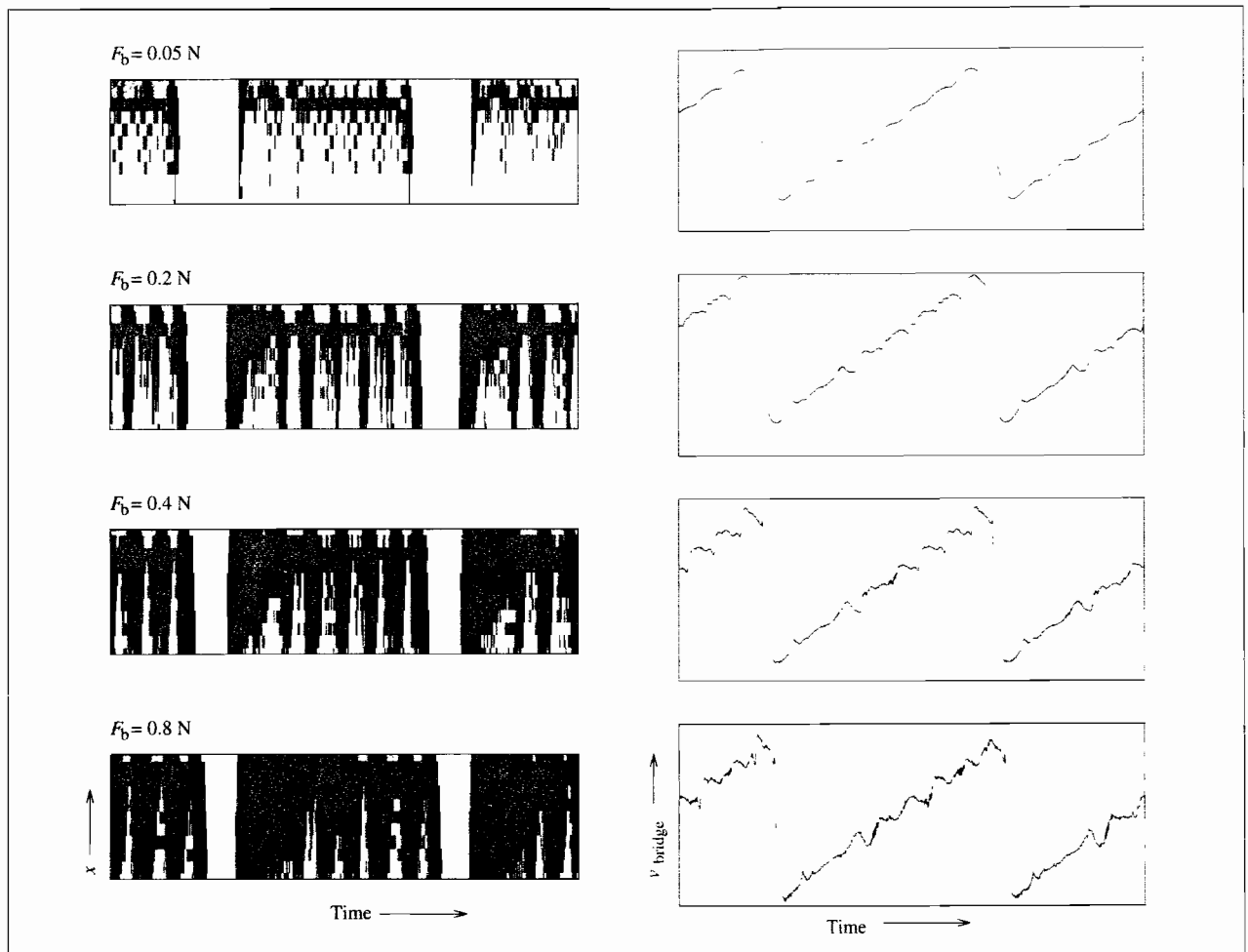
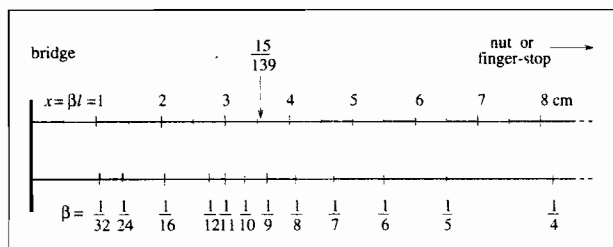
Figure 13. Friction maps and bridge-force waveforms for varying bow force F_b .

Figure 14. Position of the bow in the simulation runs of Figure 15.

With increasing bow force, the overall amplitude increases, the sawtooth becomes steeper and sharper, and the secondary waves (see Section 4.2) become more vigorous. Qualitatively, all these changes are familiar from point-bow models. Unique to the finite-width model are the changes which the individual secondary waves undergo as the bow force is increased. The important differences between point-bow and finite-width models regarding secondary waves are discussed in Section 4.2; the behaviour at the threshold of the maximum bow force will be investigated in Part III.

At very high bow forces both the point-bow and the finite-width models predict main slip durations of $T_{\text{slip}} \approx \beta T_0$. At

low bow forces the finite-width model predicts considerably longer main slips than the point-bow model, the difference between the models increasing as the bow force decreases. The waveforms produced by the finite-width model are much rounder. The longer slipping phase is not explained by the position of the "effective" bowing point (see Section 4.2) which lies further from the bridge than that of the point-bow. A shift in "effective" bowing position by $b/4$, say, would prolong the slipping phase by approximately $0.5 b/2l \approx 0.75\%$ of T_0 . Unlike the point-bow model the finite-width model predicts asymmetry of the centre-line velocity waveform about the mid-point of the slipping phase even for very low bow forces.

Figure 15 shows a series of results from simulations in which the relative bowing position β is varied. The sketch in Figure 14 indicates the position of the bow in these simulation runs. For each β a bow force with 0.8 of the value of the Schelleng maximum (equation (18)) is applied. With increasing bow-bridge distance (keeping the bow velocity constant), the strength of the incompatibility decreases, leading to fewer partial slips. The partial slips produce sharp spikes in the bridge-force waveform when the bow is close to the bridge and milder disturbances when the bow is further away from the bridge.

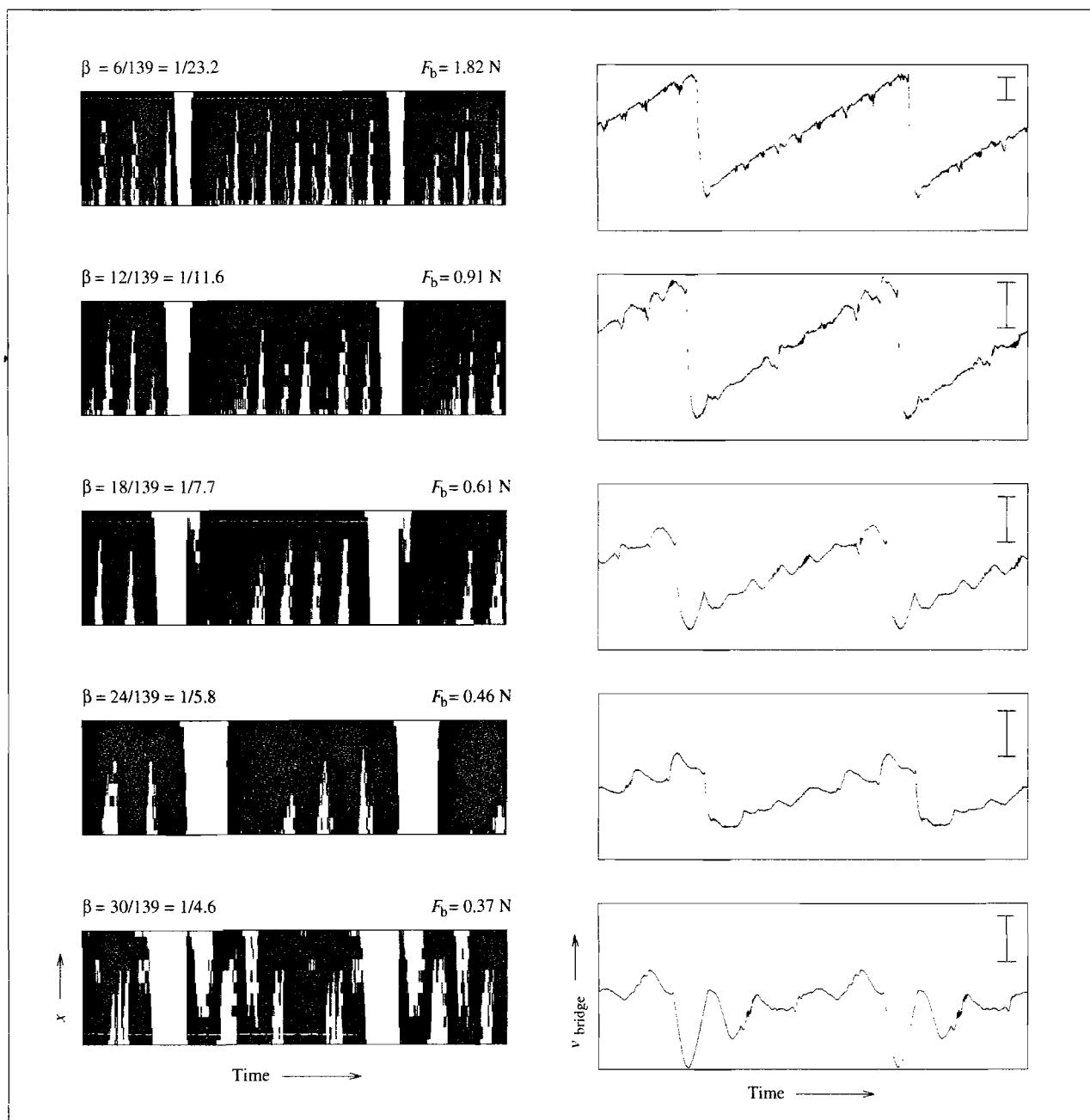


Figure 15. Friction maps and bridge-force waveforms for varying bow position (β of the bow mid-point). The vertical bars in the bridge-force plots indicate the relative scales.

When bowing close to a node perturbations of the usual bridge-force waveform can develop which dominate its shape. In the fifth case of Figure 15 the perturbations are so strong that they produce incompatibility effects and partial slips on both sides of the bow. The bow is positioned close to $\beta = 2/9$. The numerator and denominator being even and odd integers respectively, the transverse perturbations generated at release and capture, after their return from the string terminations, arrive at the bow roughly in anti-phase. This determines the pattern of the forward and backward partial slips: the slips alternate between the two edges of the bow. This case would perhaps be best classified as one of the "higher types" of periodic motion described by Raman [14].

4.2. Secondary waves and partial slips

The bridge-force waveform deduced from idealised Helmholtz motion is a perfect sawtooth (Figure 2), independent of bow force or bow velocity. However, on a real bowed string the presence of waves secondary to the Helmholtz motion modifies the bridge-force waveform. These modifications are influenced by the bowing parameters such as bow force, bow velocity, bow width and so on. Since the bridge-force waveform is ultimately responsible for the sound of the violin, it is obviously important to understand these influences.

To study the pattern of secondary waves on a real string through observation of the string velocity at a single point is difficult, because left- and right-travelling waves are superimposed, and the necessary separation is a non-trivial task. The bridge force, however, provides us with a reasonably good analogue to the travelling velocity wave emanating from the inner edge of the bow. A simulation model using travelling-wave solutions to describe the motion of the free string is a mirror image of the real situation: the separated velocity waveforms are calculated as a matter of course but the bridge force is not. We therefore analyse the velocity waveform in lieu of the bridge force.

The secondary waves are transverse and torsional waves shuttling back and forth on the string, superimposed onto the underlying periodic round-trip motion of the Helmholtz corner. In most musically acceptable vibration regimes the relevant secondary waves have amplitudes which are only a small fraction ($< 10\%$) of the amplitude of the Helmholtz motion, and time-scales which are small fractions of the period. Secondary waves with time-scales in excess of the period exist, the "ghostly subharmonics" for example [6], but these are not the concern of the present analysis. The secondary waves with time-scales smaller than the period are Schelleng's "ripples", and perturbations generated by partial slips. Schelleng's ripples are fairly well understood linear phenomena; the understanding of partial slips is still in the making.

Schelleng's ripples were first reported by Kohut and Mathews [15] and later explained by Schelleng [12]. They are generated at release and capture when the rounded Helmholtz corner interacts with the bow. Let us focus on transverse ripples first. The arrival of the rounded corner at the bow cannot trigger release (or capture) instantaneously, and thus a reflected transverse wave is generated during the build-up of the friction force before release (or capture) occurs. Transverse release ripples are trapped and repeatedly reflected between the sticking bow and the nut, capture ripples are trapped between bridge and bow. Every release and every capture generates one ripple, but due to multiple reflections a series of ripples with a time separation of βT_0 is observed at any point on the string. The perturbations of the top waveform in Figure 13 are typical Schelleng ripples. In practice, due to dispersion, dissipation and scattering into torsional waves at the bow, each individual perturbation diminishes in time. Note that when we observe the ripples on the string between bow and nut the ripples seem to grow during the sticking phase. However, the last ripple in the sticking phase is the youngest and, having been reflected only once, the strongest. Earlier ripples are older and therefore more strongly attenuated.

The Helmholtz corner also generates torsional ripples: two ripples are produced at each passage, one travelling ahead of the Helmholtz corner, one travelling in the opposite direction. (The torsional wave speed is usually greater than the transverse wave speed.) The amplitude of these ripples at generation can be estimated using the results of Part I. To a first approximation their amplitude is Z_0/Z_T times the amplitude of the corresponding transverse ripple.

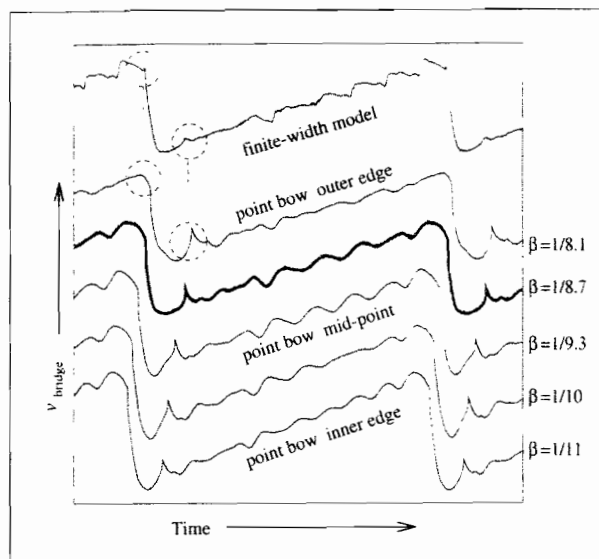


Figure 16. Bridge-force waveforms of the finite-width model (top trace) and the point-bow model with β corresponding to five different positions under the finite-width bow. Waveforms shifted horizontally and vertically for presentational purposes. Time window $1.5 T_0$.

At each arrival of a ripple at the bow, reflection and transmission take place so that we cannot consider the two sides of the bow independently. In addition, transverse waves scatter into reflected and transmitted torsional ones, and vice versa. This multiple-scattering behaviour was described by Cremer [3], and treated in some detail in a study of stability by Woodhouse [16].

In addition to these linear reflection and transmission phenomena the interaction of release and capture ripples with the bow can be complicated by partial slips. Partial slips then generate further secondary waves, both transverse and torsional, which also shuttle back and forth between the bow and the terminations of the string. If a partial slip coincides with the arrival of a ripple at the bow then the scattering of the ripple is no longer a linear process. The stick-slip process and the scattering process become intertwined in a complicated way. This is true regardless of whether the (partial) stick-slip transitions are triggered by the ripple or by some other mechanism.

4.3. Miniature Helmholtz motion

This complicated situation can be illustrated by a computed example. It is illuminating to use a point-bow simulation with input parameters similar to those of the finite-width reference case and compare details. The waveforms of point-bow simulations are easier to understand because they are free from the effects of partial slips. In Figure 16 are shown the bridge-force waveforms of the reference case and of point-bow calculations at five bow positions spaced at $b/4$ intervals within the finite width. Both types of calculation employ the same friction law. The distributed bow-hair impedance of the finite-width case is lumped into an equivalent point impedance.

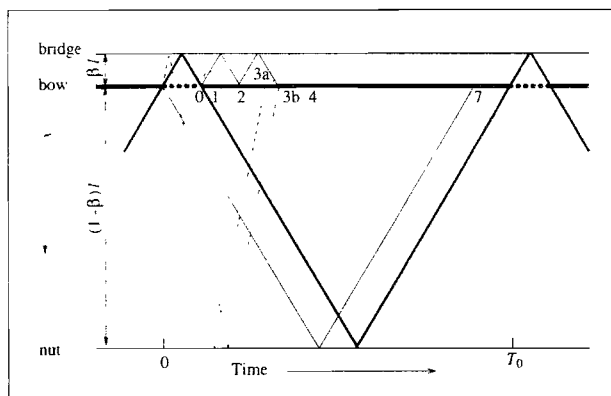


Figure 17. Space-time diagram indicating the paths of some of the main perturbations in the computed cases. Heavy line: the path of the Helmholtz corner. Solid lines: paths of transverse release and capture ripples. Dashed lines: paths of torsional release and capture ripples. (See text.)

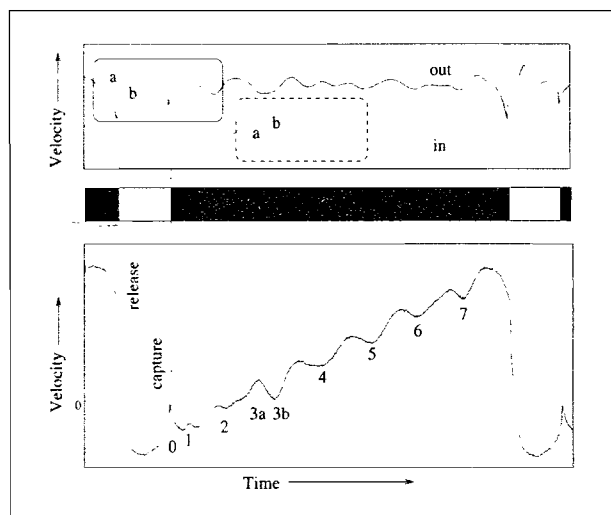


Figure 18. Point-bow model with $\beta = 1/8.7$. Top traces: torsional velocity wave emanating from the bow towards the nut (solid line) and returning to the bow after reflection at the nut (dashed line). Middle: friction map. Bottom trace: bridge-force waveform. (Note that the bottom trace is really the outgoing velocity wave from the inner bow hair, so that it is time-shifted relative to the actual bridge force.) Time window $1.25 T_0$.

The closest resemblance to the finite-width case is found for the point-bow at $\beta = 1/8.7$, the case given by the heavy line. It is closest in overall amplitude, in duration of the nominal slipping phase, and in pattern of the secondary waves. This particular point bow lies within the part of the finite width for which the string is actually sticking throughout the nominal Helmholtz sticking phase. However, the similarity of the finite-width model and the point-bow model with this "effective" β cannot be stretched very far; for example parameter studies in which the bow force is varied reveal that the point-bow model has a maximum bow force which is much lower than that of the finite-width model.

Which are the secondary waves that determine the pattern of perturbations seen in the waveforms of Figure 16?

To enable us to answer this question a space-time diagram is provided in Figure 17 indicating the paths of the main secondary waves in the computed cases. The individual secondary waves which affect the bridge-force waveform are easy to trace for the point-bow model. Once the relevant secondary waves are identified for the point bow we can turn to the finite-width results.

Figure 18 shows the bridge-force waveform highlighted in Figure 16 in more detail and in addition the torsional velocity waves travelling between bow and bridge.

Ripple 0, the first significant event seen in the bridge-force waveform after release, is the transverse capture ripple. Ripple 1 is the transverse motion generated by the torsional capture ripple returning from the bridge and interacting with the sticking bow. Most of its energy is converted into a transmitted torsional wave and a reflected transverse wave. The rather small reflected torsional wave, trapped between bow and bridge, quickly becomes insignificant and its effect is not seen at later times. Ripple 2 is the effect of the first return of the transverse capture ripple reflected at the bridge. Ripple 3a is the effect of the torsional release ripple a, returning from the nut. It is followed, with a delay of $\beta T_0 (c_0/c_T)$, by ripple 3b, the effect of the forward torsional release ripple b, having been reflected first at the bridge and then at the nut. Superimposed onto this is the effect of the transverse release ripple 3c after its second reflection at the bridge. This combination of waves incident at the bow accounts for the relatively large amplitude of the "compound ripple" 3a–3c. The compound ripple returning from the bridge generates ripple 4. Ripples 5–7 have the typical βT_0 -spacing. They result from the superposition of the standard transverse release ripples generated in this and the preceding two periods and trapped between bow and nut, and the compound ripple which is trapped between bridge and bow and repeatedly reflected at bridge and bow.

We now make a corresponding examination of the finite-width case, shown in Figure 19. The first observation is that the finite-width case produces release and capture ripples, transverse and torsional, with smaller amplitudes than the point-bow case (compare ripples a, b and 0 in Figures 18 and 19). Both linear and nonlinear effects contribute to this. Firstly, the finite-width bow is more permeable for incident waves than the point bow and this reduces the amplitude of any reflected wave. Secondly, the string unzips and re-zips gradually as opposed to instantaneously in the point-bow case. Therefore the friction force does not reach the same levels as in the point-bow case and it drops less quickly after the transition. As a consequence the release and capture ripples are less sharp and have smaller amplitudes.

The reduced size of ripples generated by a finite-width bow may be relevant to a phenomenon observed previously. If a string is bowed with a wooden rod coated with rosin, Helmholtz motion can be generated much as with a normal bow. However, the resulting sound is quite different: it is harsher and more strident. The change in spectral content associated with larger ripples may be partly responsible for this (although the relatively irregular distribution of rosin on the rod may also be a significant factor).

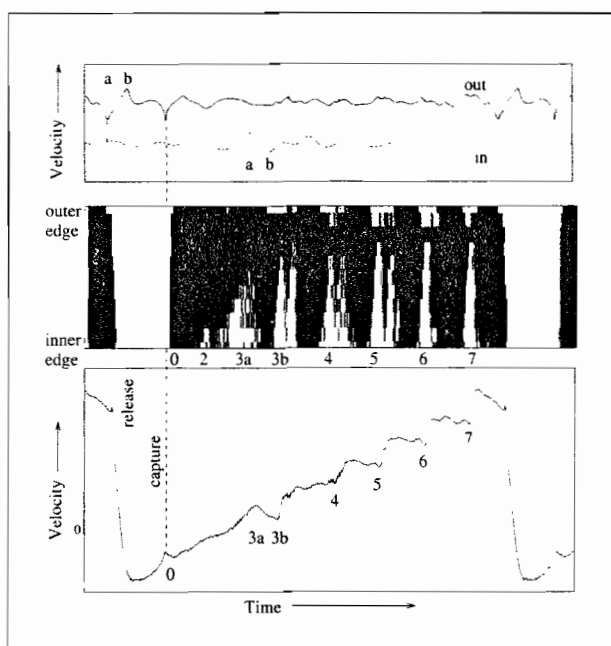


Figure 19. Finite-width model. Top traces: torsional velocity wave emanating from the bow towards the nut (solid line) and returning to the bow after reflection at the nut (dashed line). Middle: friction map. Bottom trace: bridge-force waveform. Time window $1.25 T_0$.

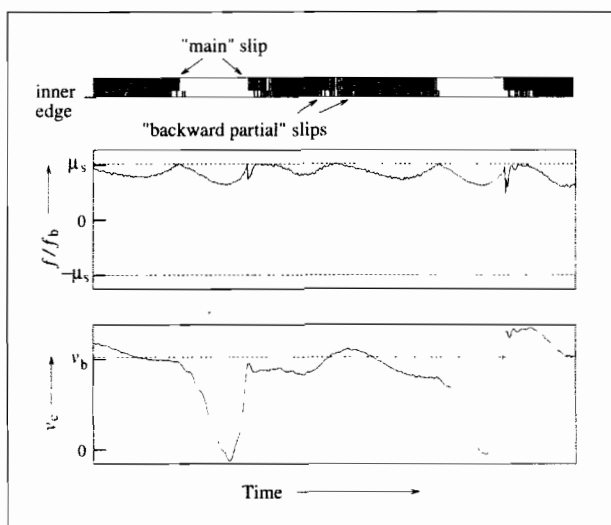


Figure 20. The miniature Helmholtz motion of the partial slips. Top: friction map of the first 1.5 mm of the bow width at the inner edge. Middle and bottom traces: friction force and string centre-line velocity v_c at the inner edge of the bow respectively. All plots are enlargements of parts of the plots in Figure 10. Time window $2\beta T_0$.

In the point-bow case the two torsional ripples generated at release (or capture) and travelling in opposite directions have the same amplitude: they are both generated by the same friction force applied at the bowed point and the torsional behaviour is symmetric about that point as long as there is no significant incident torsional wave at the time of release (or capture). Not so in the finite-width case: the nut-side torsional release and capture ripples have larger amplitudes than the bridge-side ripples.

The smaller amplitudes of the release and capture ripples explain the absence of ripples 1 and 2 in the bridge-force waveform of the finite-width case. The transverse capture ripple does, however, trigger partial slip 2 at the inner edge. This partial slip is weak and does not result in any significant perturbation of the bridge-force waveform. The compound ripple 3a–3c of the point-bow model is found to have a reduced amplitude in the finite-width case because the two torsional release ripples a and b have smaller amplitudes and because the contribution from the transverse capture ripple is missing.

Partial slips 4–7 at the inner edge are mainly the effect of the transverse release ripples (trapped between bow and nut) and the compound ripple trapped between bridge and bow. Each partial slip at the inner edge of the bow can be matched to a perturbation in the bridge-force waveform. The ripples of the point-bow case are sharpened in the finite-width case by the spiky components resulting from the partial slip mechanism. The details of these partial slips are influenced by the torsional waves already present on the string before partial slip 4 and the release and capture ripples generated by the partial slips themselves.

This particular finite-width case is one in which a “miniature Helmholtz motion” is set up between bow and bridge. From partial slip 4 onwards a regular pattern has been set up. The spacing between subsequent partial slips corresponds to the travel time for a transverse perturbation to perform the round-trip between bridge and the part of the string which remains in sticking contact with the bow throughout the nominal sticking phase. (The spacing between subsequent partial slips is measured as the time between subsequent releases of the string at the first grid-point completely within the bow, as the interface grid-point is subject to small disturbances which can produce localised slips but are of minor interest in this context.) The impulse generated by one partial slip triggers the next partial slip after one round trip. Similar to the main slip, release in partial slips takes about twice as long as capture.

Details of the miniature Helmholtz motion are presented in Figure 20. The time window has been shortened by a factor of β . The friction map corresponds to the grid-points representing the first 1.5 mm of the bow at the inner edge. The size and position of the enlarged area with respect to the full-scale Helmholtz motion are shown in Figure 10. The vertical scale in the plot of the string centre-line velocity at the inner edge is magnified by a factor of $1/\beta$. The resemblance of the small-scale and the full-scale contact mechanics is very clear. Whether this miniature Helmholtz motion with its time-keeping mechanism occurs or not depends on the combination of the input parameters v_b , f_b and β .

On a real bowed string the sequence of partial slips is likely to be less regular than in these steady-state simulations. Additional perturbations, be it in the bow velocity, the bow force (bow and string vibration in the perpendicular plane) or any other relevant quantity, may render the timing of the partial slips aperiodic. It is clear, however, that finite bow width by way of the particular pattern of partial slips can shape the bridge-force waveform in significant ways.

5. Conclusions

A model has been developed to describe the excitation of a string by a bow of finite width. Some representative results have been computed and discussed. Many aspects of the behaviour are qualitatively familiar from earlier point-bow studies. However, they are modified in detailed ways which are likely to be psychoacoustically relevant in a real violin. In addition, new effects are seen which do not arise with a point bow. Principal among these is the phenomenon of "partial slipping", in which some bow-hairs slip while others continue to stick to the string during the nominal sticking phase of the Helmholtz motion. These have been discussed earlier in the context of a more primitive model, but a realistic account of their detailed pattern was not possible before the present model was developed. A more comprehensive discussion of the results will be given in Part III [7].

References

- [1] R. Pitteroff, J. Woodhouse: Mechanics of the contact area between bow and string. Part I: Reflection and transmission behaviour. *Acustica - acta acustica* **84** (1998) 543–562.
- [2] F. L. W. Reinicke: Die Übertragungseigenschaften des Streichinstrumentensteges. Dissertation. Technische Universität Berlin, 1973.
- [3] L. Cremer: The physics of the violin. MIT Press, Cambridge, MA, USA, 1985.
- [4] M. E. McIntyre, R. T. Schumacher, J. Woodhouse: On the oscillations of musical instruments. *J. Acoust. Soc. Am.* **74** (1983) 1325–1345.
- [5] M. E. McIntyre, R. T. Schumacher, J. Woodhouse: Aperiodicity in bowed-string motion. *Acustica* **49** (1981) 13–32. See also next reference.
- [6] M. E. McIntyre, R. T. Schumacher, J. Woodhouse: Aperiodicity in bowed-string motion: On the differential-slipping mechanism. *Acustica* **50** (1982) 294–295.
- [7] R. Pitteroff, J. Woodhouse: Mechanics of the contact area between bow and string. Part III: Parameter dependence. *Acustica - acta acustica* (1998). accepted for publication.
- [8] H. Lazarus: Die Behandlung der selbsterregten Kippschwingung der gestrichenen Saite mit Hilfe der endlichen Laplace-transformation. Dissertation. Technische Universität Berlin, 1972.
- [9] J. H. Smith: Slip and stick vibration and its constitutive laws. Dissertation. University of Cambridge, 1990.
- [10] R. Pitteroff: Contact mechanics of the bowed string. Dissertation. University of Cambridge, 1995.
- [11] J. Woodhouse: On the playability of violins. Part I: Reflection functions. *Acustica* **78** (1993) 125–136.
- [12] J. C. Schelleng: The bowed string and the player. *J. Acoust. Soc. Am.* **53** (1973) 26–41.
- [13] R. T. Schumacher: Measurements of some parameters of bowing. *J. Acoust. Soc. Am.* **96** (1994) 1985–1998.
- [14] C. V. Raman: On the mechanical theory of bowed strings and of musical instruments of the violin family, with experimental verification of results: Part I. *Bull. Indian Ass. Cult. Sci.* **15** (1915) 1–158.
- [15] J. Kohut, M. V. Mathews: Study of motion of a bowed violin string. *J. Acoust. Soc. Am.* **49** (1971) 532–537.
- [16] J. Woodhouse: On the stability of bowed string motion. *Acustica* **80** (1994) 58–72.